

Dust in the Wolf-Rayet nebula M 1-67

P. Jiménez-Hernández^{*}, S.J. Arthur and J.A. Toalá

Instituto de Radioastronomía y Astrofísica (IRyA), UNAM Campus Morelia, Apartado postal 3-72, 58090 Morelia, Michoacan, Mexico

25 February 2022

ABSTRACT

The Wolf-Rayet nebula M 1-67 around WR 124 is located above the Galactic plane in a region mostly empty of interstellar medium, which makes it the perfect target to study the mass-loss episodes associated with the late stages of massive star evolution. Archive photometric observations from *WISE*, *Spitzer* (MIPS) and *Herschel* (PACS and SPIRE) are used to construct the spectral energy distribution (SED) of the nebula in the wavelength range of 12–500 μm . The infrared (photometric and spectroscopic) data and nebular optical data from the literature are modeled simultaneously using the spectral synthesis code *CLOUDY*, where the free parameters are the gas density distribution and the dust grain size distribution. The infrared SED can be reproduced by dust grains with two size distributions: a MRN power-law distribution with grain sizes between 0.005 and 0.05 μm and a population of large grains with representative size 0.9 μm . The latter points towards an eruptive origin for the formation of M 1-67. The model predicts a nebular ionized gas mass of $M_{\text{ion}} = 9.2^{+1.6}_{-1.5} M_{\odot}$ and the estimated mass-loss rate during the dust-formation period is $\dot{M} \approx 6 \times 10^{-4} M_{\odot} \text{ yr}^{-1}$. We discuss the implications of our results in the context of single and binary stellar evolution and propose that M 1-67 represents the best candidate for a post-common envelope scenario in massive stars.

Key words: Massive stars — stars: evolution — stars: circumstellar matter — stars: individual (WR124) — stars: mass loss

1 INTRODUCTION

Wolf-Rayet (WR) stars represent the most advanced evolutionary stage of very massive stars prior to supernova explosion ($M_i \gtrsim 25 M_{\odot}$; Langer 1995; Ekström et al. 2012). Mass loss is important at all stages of a massive star’s life and the WR stage corresponds to the He-rich core once the outer envelope has been stripped away. In the single massive star scenario, O stars with initial masses $25 M_{\odot} < M_i < 60 M_{\odot}$ evolve into a red supergiant (RSG) stage exhibiting slow (10–30 km s^{-1}) and dense winds ($\dot{M} \approx 10^{-4} M_{\odot} \text{ yr}^{-1}$), whilst stars with even higher initial masses ($> 60 M_{\odot}$) are thought to pass through a luminous blue variable (LBV) stage (Georgy et al. 2012), in which they experience eruptive mass-loss episodes ($\dot{M} \gtrsim 10^{-3} M_{\odot} \text{ yr}^{-1}$; Weis 2001). Finally, after losing its hydrogen-rich envelope through the RSG or LBV phase, the star exposes its hot core becoming a WR star. However, the effect of binarity on stellar evolution cannot be ignored, since most O stars are born in close binary or multiple systems (Mason et al. 2009). During the lifetime of the system, there will be some interaction before the massive star ends its life as a supernova (Sana et al. 2012). In the binary scenario, Roche lobe overflow can lead to enhanced mass loss of the primary and mass transfer to the secondary, altering the lifetimes of both components in the different evolutionary stages

(e.g., van den Heuvel & Heise 1972; de Mink et al. 2014). One of the components might have its hydrogen-rich envelope stripped completely, thereby creating a WR star (e.g., Wellstein et al. 2001).

Regardless of the WR formation process, their powerful line-driven winds ($v_{\infty} > 1000 \text{ km s}^{-1}$, $\dot{M} \approx 10^{-5} M_{\odot} \text{ yr}^{-1}$; Hamann et al. 2006) and high ionizing photon luminosity ($Q_{\text{H}} > 5 \times 10^{48} \text{ s}^{-1}$) interact with the circumstellar environment producing optical WR nebulae in many cases. Thus, the study of WR nebulae can provide information on the mass-loss history and previous evolution of the central star.

WR nebulae have been characterized through optical images and spectra. Narrow-band filter images have been used to classify their [O III], H α and [N II] morphologies into three broad classes: H II regions, ejecta nebulae and wind-blown bubbles (Chu 1981). The ejecta nebulae have clumpy or irregular nebulosity suggesting a violent mass-loss episode and are mainly associated with the late WNH spectral type (Stock & Barlow 2010), that is, the hydrogen envelope is not completely lost. Spectroscopic studies of nebular abundances show evidence of enrichment with material processed in the CNO cycle in cases where the nebula is not dominated by swept-up interstellar medium (see e.g., Esteban et al. 1991, 1992, 2016; Fernández-Martín et al. 2013).

Since the advent of infrared (IR) astronomy, thermal dust emission has been detected in the vicinity of hot stars and, specifically, in WR nebulae (van Buren & McCray 1988). In particu-

^{*} E-mail: p.jimenez@irya.unam.mx

lar, Marston (1991) analysed *IRAS* observations of the WR nebulae NGC 2359, NGC 6888 and RCW 58 around the WNE stars WR 7, and WR 136 and the WN8 star WR 40, respectively, and estimated the dust and their nebular masses in each case from the ratio of the 60 μm to 100 μm intensities. The main conclusion of Marston (1991) is that the nebular masses in each case are too large to be composed solely of material expelled from the central stars and so a sizeable proportion of the nebular mass must be due to swept-up ISM material. However, Mathis et al. (1992) also analyzed the *IRAS* data for RCW 58 and NGC 6888 with more sophisticated grain physics and grain spatial distribution and concluded that the nebular mass for RCW 58 is in fact two orders of magnitude lower than that estimated by Marston (1991) and is therefore consistent with all the nebular material having a stellar origin. More recently, Gvaramadze et al. (2010) exploited mid-IR *Spitzer Space Telescope* data to identify compact nebulae around evolved stars. Follow-up spectroscopic identification resulted in an increase in the number of known Galactic LBVs and late-type WN stars. Toalá et al. (2015) analysed the mid-IR morphologies of nebulae around WR stars using *Wide-field Infrared Survey Explorer* (*WISE*) infrared images and proposed a classification scheme that is loosely correlated with the spectral type of the central star.

Both RSG and LBV stars are known to be copious producers of dust but its production will cease as soon as the star enters the hot WR phase.¹ In RSG stars, O-rich dust, such as silicates or Al_2O_3 forms at a few stellar radii due to the condensation of molecules (see Verhoelst et al. 2009). Convection cells are thought to play an important role in levitating the molecular gas above the stellar photosphere into the upper atmosphere (Chiavassa et al. 2010). Detailed Very Large Telescope VISIR imaging studies of the nearest RSG, Betelgeuse (Kervella et al. 2011), show that the close circumstellar environment is very clumpy, suggesting inhomogeneous and episodic mass loss. From optical polarimetric imaging observations of the extreme RSG VY CMa and its clumpy, dusty circumstellar environment, Scicluna et al. (2015) derive an average grain size of $\sim 0.5 \mu\text{m}$, that is, 50 times larger than grains in the diffuse ISM, with only a small variation in grain size. The condensation of dust in the environments of the much hotter and more luminous LBV stars requires some sort of shielding from the star's UV and optical emission (Gail et al. 2005; Kochanek 2011). It has been proposed that dust formation in these objects is closely linked to the eruptive state of LBVs because only very high mass-loss rates $\dot{M} > 10^{-2.5} M_\odot \text{ yr}^{-1}$ can provide the non-dust optical depths required. The maximum grain size a_{max} is related to the mass-loss rate in this scenario (Kochanek 2011). Very large grains ($a_{\text{max}} > 1 \mu\text{m}$) have been inferred for η Carinae (Morris et al. 2017). Studies of very young WR nebulae, or nebulae in low density environments far from the Galactic plane which are not dominated by swept-up ISM material, should be able to shed some light on the history of the dust formation process in the previous evolutionary stage.

We have selected the iconic WR nebula M1-67 around the late-type WN star WR 124 (also known as 209 BAC or Merrill's star) as an ideal object to study the dust properties of the circumstellar nebula. It has Galactic latitude $b = 3.31^\circ$, which places it at $z \sim 370 \text{ pc}$ above the Galactic plane for an assumed distance of 6.4 kpc (see Appendix A). At this position the interstellar medium density is low enough that the nebula is expected to be composed almost entirely of material expelled from the progenitor of WR 124.

M1-67 and its central star have been objects of many studies. WR 124 was identified as a high-velocity late-type WN star by Merrill (1938) who suggested an association with planetary nebulae based on the high velocity (see also Perek & Kohoutek 1967). Minkowski (1946) discovered the clumpy $\text{H}\alpha$ emission nebula on photographic plates and it was denominated M1-67² and classified as a planetary nebula based on appearance. Later Cohen & Barlow (1975) demonstrated, using primarily extinction arguments, that Merrill's Star and M1-67 must be a Population I WN8 star and its associated ring nebula. Solf & Carsenty (1982) showed that the $\text{H}\alpha$, [N II] and [S II] velocity fields of the nebula obtained from long-slit spectra can be explained by a nearly spherical thin shell of numerous condensations expanding at 46 km s^{-1} with respect to a common centre. The centre of the expansion has a heliocentric velocity of 158 km s^{-1} , very similar to the radial velocity of the central star ($175\text{--}200 \text{ km s}^{-1}$). This is consistent with the ejecta nebula scenario proposed by Chu & Treffers (1981). A more complex dynamical structure, consisting of an expanding hollow spherical shell ($v = 46 \text{ km s}^{-1}$) and a bipolar outflow ($v = 88 \text{ km s}^{-1}$) was reported from a long-slit spectrographic study by Sirianni et al. (1998). Although M1-67 appears symmetric and almost spherical (or hexagonal) in $\text{H}\alpha$ images, with the star at the centre of the $\sim 110''$ diameter nebula (Grosdidier et al. 1998), high contrast coronagraphic studies (Nota et al. 1995) of the inner regions do reveal a bipolar structure, which is also evident in *Spitzer* 24 μm images (Gvaramadze et al. 2010). This has been attributed to anisotropic outbursts such as are seen in LBV (Nota 1999).

Spectra of M1-67 show strong [N II] and $\text{H}\alpha$ nebular lines but [O III] is almost completely absent (see e.g., Esteban et al. 1991). Abundance determinations find that N is enhanced, O is deficient and S has normal H II region abundances. This is further evidence that WR124 had a massive progenitor since these abundances are an indication of material processed in the CNO cycle and it reinforces the idea that there has been no significant interaction with the ISM. Moreover, the physical conditions in the nebula are found to be consistent with a very low ionization level, and an electron temperature $T_e \sim 6200$ to 8200 K (Esteban et al. 1991; Fernández-Martín et al. 2013).

The distance to WR 124 and M1-67 is not well determined and has been a subject of discussion. Extinction studies put a lower limit to the distance of 2.5 kpc (Esteban et al. 1991), while a spectrophotometric distance of 8.4 kpc was determined by Hamann et al. (2006). On the other hand, Marchenko et al. (2010) used multi-epoch *Hubble Space Telescope* (*HST*) images to estimate a geometric distance of $3.35 \pm 0.67 \text{ kpc}$ to M1-67. The recent *Gaia* Data Release 2 provides 5-parameter astrometric data for WR 124 (positions, parallax and proper motions), which can be combined to estimate the distance using Bayesian methods (Bailer-Jones et al. 2018; Luri et al. 2018). Recently, Rate & Crowther (2020) presented a method to estimate distances to WR stars using the *Gaia* data including the *G*-band photometry and estimated a distance of 5.9 kpc for WR 124 using a prior based on H II regions and dust extinction. We performed our own calculation using the *Gaia* data and a different prior and obtained 6.4 kpc. In Appendix A we describe the details of this procedure and show that both distances are consistent within the estimated error values. Following our result, in this paper we adopt 6.4 kpc as the distance to WR 124 and its nebula. At this distance, the 110 arcsec diameter of the nebula corresponds to a spatial size of 3.4 pc.

¹ Dust can be also produced in the dense interaction region of colliding wind WC binary systems.

² Object 67 in Table 1 of Minkowski (1946)

Instrument	Date (yyyy-mm-dd)	Obs. ID	PI	λ_c or $\Delta\lambda$ (μm)	Duration (s)	Processing level
<i>WISE</i>	2010-04-11	2876p166_ac51		12 (W3), 22 (W4)	8.8	Level 3
<i>Spitzer</i> MIPS	2006-10-15	30544	Morris, P.	24	3	Level 2
<i>Herschel</i> PACS	2010-04-08	1342194080	Groenewegen, M.A.T.	70, 160	2622	Level 3
		1342194082	Groenewegen, M.A.T.	100, 160	2622	Level 3
<i>Herschel</i> SPIRE	2010-09-21	1342204949	Groenewegen, M.A.T.	250, 350, 500	911	Level 2
<i>Spitzer</i> IRS	2004-04-19	199	Houck, J.R.	7.53–14.73 (SL1)	121.9	Level2
				14.27–21.05 (LL2)	94.4	
				20.56–38.42 (LL1)	94.4	

Table 1. Details of the IR observations used in this paper.

Vamvatira-Nakou et al. (2016) presented *Herschel* imaging and spectroscopic observations of M 1-67. A comparison of the infrared images with optical images shows that the dust nebula coincides with the ionized gas, indicating that the dust and gas are mixed. Vamvatira-Nakou et al. (2016) used the 2-Dust code (Ueta & Meixner 2003) to model the dust emission and concluded that two populations of dust grains were required to produce the infrared spectral energy distribution (SED). The total mass of dust resulting from their model is $0.22 M_{\odot}$ of which $0.21 M_{\odot}$ corresponds to the population of large grains with radii from 2 to $10 \mu\text{m}$. They conclude that the progenitor of WR 124 was a RSG with initial mass $\sim 32 M_{\odot}$. However, such large grain sizes are not consistent with observations of nearby RSG (Scicluna et al. 2015) and such a low progenitor mass is not consistent with an LBV origin for the nebula, such has been proposed by several authors (see, e.g., Sirianni et al. 1998; Fernández-Martín et al. 2013).

In this paper, we perform a detailed characterization of the dust in M 1-67 by analysing *WISE*, *Spitzer* and *Herschel* observations and using the spectral synthesis code CLOUDY (Ferland et al. 2017) to fit simultaneously the dust photometric data and nebular optical data from the literature. This paper is organized as follows: in Section 2 we describe the observations used and detail the IR photometry. In Section 3 we describe our photoionization model obtained with CLOUDY and the results of the models are given in Section 4. The discussion and summary are presented in Section 5 and 6, respectively.

2 OBSERVATIONS AND IR PHOTOMETRY

2.1 Observational Data

We use public IR observations (images and spectroscopy) from a variety of IR satellites. All observations were retrieved from the NASA/IPAC Infrared Science Archive³.

We obtained IR images of M 1-67 from *WISE*, *Spitzer* (MIPS) and *Herschel* (PACS and SPIRE)⁴. The combination of all these observations give us a wide view of M 1-67 covering the 12–500 μm wavelength range and enable us to construct a detailed SED. Although *Spitzer* IRAC observations are available, those images are contaminated by the presence of a large number of stars in the field of view of M 1-67, which complicates the photometry extraction. Details of the individual observations are provided in Table 1.

³ <https://irsa.ipac.caltech.edu/frontpage/>

⁴ The *Herschel* observations were obtained as part of the Mass-loss of Evolved Stars (MESS) project (Groenewegen et al. 2011).

Figure 1 shows all of the IR images obtained from *WISE*, *Spitzer* (MIPS) and *Herschel* (PACS and SPIRE). These IR images clearly show a bipolar morphology (see, e.g., Sirianni et al. 1998), in contrast to the symmetrical nebula seen in deep *HST* WFPC2 *H α* image of M 1-67 (Grosdidier et al. 1998). This is appreciated to some extent even in the long wavelength *Herschel* SPIRE images (bottom row of Fig. 1). Some extended emission can be seen in the *WISE* 12 μm and the *Herschel* SPIRE images, which is very likely to be contribution from material in the line of sight rather than material at the location of M 1-67, given its position above the Galactic plane.

We also obtained *Spitzer* Infrared Spectrograph (IRS) low-resolution data, which cover a spectral range of 7–38 μm . These observations were processed using the CUBE Builder for IRS Spectral Maps (CUBISM; Smith et al. 2007).

2.2 IR photometry

In order to extract a SED from M 1-67, we defined a region that encompasses the nebular emission for each individual IR image. We then integrated the flux density for each region so defined. A background correction was applied to the flux value from each image. The background is not uniform and is different at each wavelength. Thus, the selected background regions for each IR image are not the same as those for a different image. The backgrounds were selected by eye and a set of n -background regions was obtained for each image. We subtracted each background from the nebular flux density in order to obtain n background-subtracted fluxes for each IR wavelength image. The mean and standard deviation of these values then give us the final flux value and measurement uncertainty (σ_{back}), respectively. Figure 2 shows an example of the background selection process.

To calculate the total error from each IR band we add together the different contributions, as well as the uncertainty due to the background subtraction. The calibration uncertainty (σ_{cal}) from each instrument has to be taken into account, too. Then, the total error is given by

$$\sigma_{\text{Tot}} = \sqrt{\sigma_{\text{back}}^2 + \sigma_{\text{cal}}^2}. \quad (1)$$

For the *WISE* data, the calibration uncertainty is 4.5% and 5.7% from the W3 and W4 bands, respectively. The *Herschel* data calibration uncertainty is 5% for the PACS and 7% for the SPIRE instruments, while that for the *Spitzer* MIPS is 4%.

We note that the photometry of M 1-67 extracted from the *WISE* W3 band has a significant contribution from the central star, WR 124. We carefully subtracted the contribution from WR 124 by

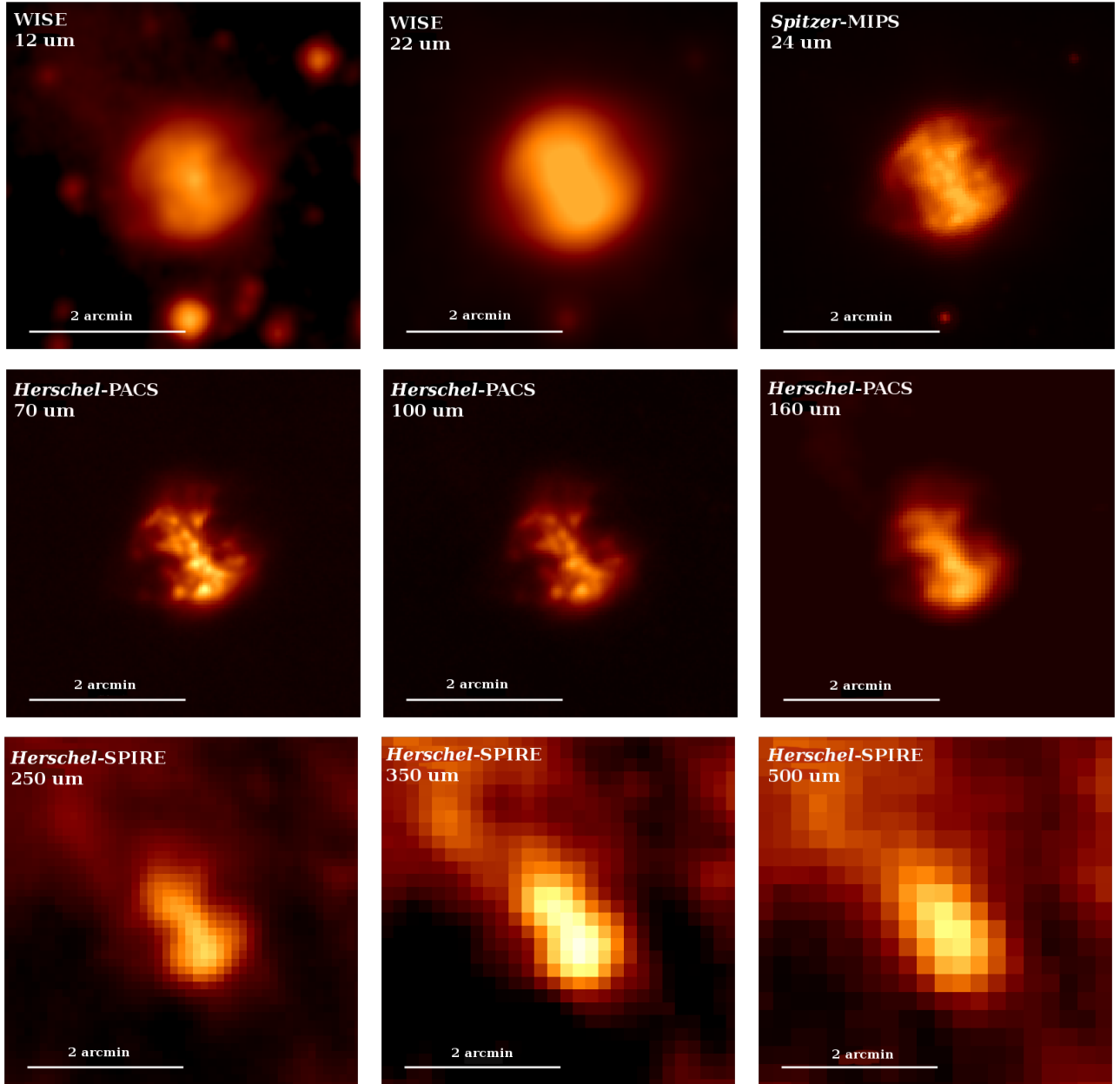


Figure 1. Images of the nebula M 1-67 obtained by *WISE*, *Spitzer* and *Herschel*. The different bands are centered at 12, 22, 24, 70, 100, 160, 250, 350 and 500 μm . North is up and east to the left.

comparing the PSF of stars in the field. This produced a clean photometric measure of the W3 12 μm band.

In Table 2 we present the final flux estimates for each IR image of M 1-67 with their corresponding uncertainties (σ_{Tot}) associated with the instrument calibration and the background subtraction process. The final IR SED of M 1-67 is presented in Figure 3.

2.3 Modified Black Body Model

A modified black body fit (MBB) to the dust emission in the far infrared ($\lambda \geq 100 \mu\text{m}$) is a useful tool for estimating the dust mass and mean dust temperature of the coolest, i.e., the largest dust grains in M 1-67. The underlying assumption is that the dust is optically thin in local thermodynamic equilibrium (LTE) and that a single tem-

perature T_{D} and emissivity index β are representative of all the dust grains. The MBB fit to the observed flux densities is

$$F_{\nu} = M_{\text{D}} \kappa_{\nu} \frac{B_{\nu}(T_{\text{D}})}{d^2}, \quad (2)$$

where d is the distance to the nebula, $B_{\nu}(T_{\text{D}})$ is the Planck function and M_{D} is the total dust mass. The dust emissivity κ_{ν} is an exponential function of frequency parametrized by the emissivity index β , that is

$$\kappa_{\nu} = \kappa_{\nu_0} \left(\frac{\nu}{\nu_0} \right)^{\beta}. \quad (3)$$

The dust emissivity normalization for $R_{\text{V}} = 3.1$ Milky Way dust is $\kappa_{\nu_0} = 1.92 \text{ cm}^2 \text{ g}^{-1}$ at the reference wavelength $\nu_0 = 350 \mu\text{m}$ (Draine 2003).

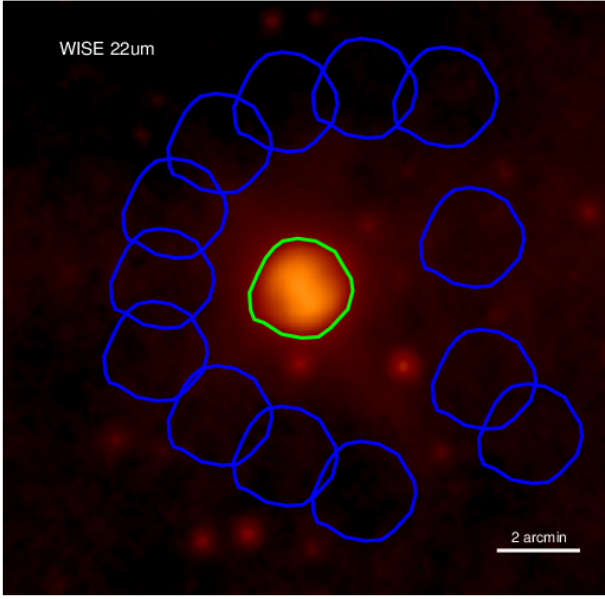


Figure 2. Examples of background selection regions around M 1-67. The image shows the *WISE* band 4. The region used for extracting the flux from M 1-67 is shown with a green contour and the background regions are shown in blue.

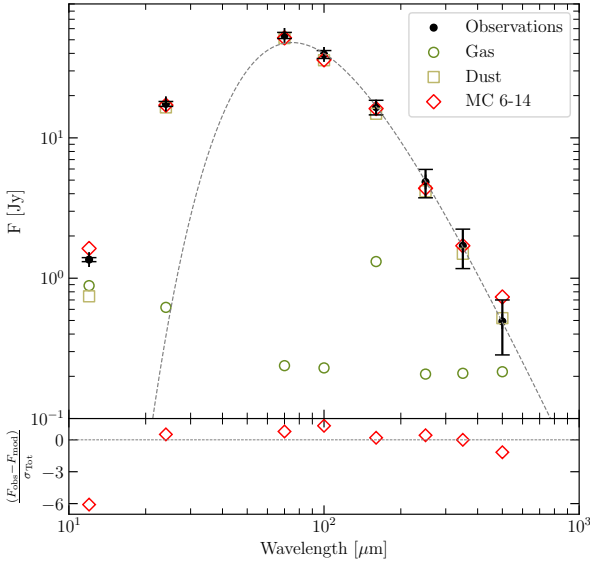


Figure 3. SED obtained from the IR observations of M 1-67: (black) dots (see Table 2). The error bars take into account uncertainties associated with the instrument calibration and the background subtraction process. The synthetic SED obtained from our best model, MC 06-14, is also shown with empty red diamonds (see Section 4.2 for details). The contribution to the synthetic photometry from the ionized gas and dust are also shown. The residual is defined as $(F_{\text{obs}} - F_{\text{mod}})/\sigma_{\text{Tot}}$. The dashed line shows the best fit (for $\lambda \geq 100\mu\text{m}$) to the *Herschel* PACS and SPIRE photometry for a modified black body model, see Section 2.3 for details

Instrument	λ_c [μm]	Flux [Jy]	σ_f	σ_{cal}	σ_{Tot}
<i>WISE</i>	12	1.36	0.05	0.06	0.08
	22	17.91	0.04	1.02	1.80
<i>Spitzer</i> MIPS	24	17.47	0.08	0.70	0.7
<i>Herschel</i> PACS	70	53.72	0.25	2.69	2.70
	100	39.34	1.62	1.97	2.55
<i>Herschel</i> SPIRE	160	16.55	1.79	0.83	1.98
	250	4.85	1.06	0.34	1.11
	350	1.70	0.53	0.12	0.53
	500	0.49	0.21	0.03	0.21

Table 2. Flux densities and uncertainties of different IR band observations of M 1-67. σ_f is the uncertainty associated with background inhomogeneity, σ_{cal} is the uncertainty associated with the instrument calibration of each observation and σ_{Tot} is the sum of these uncertainties.

The MBB fit returns the dust temperature T_D and the emissivity index β of the grains responsible for the emission at wavelengths $\lambda \geq 100\mu\text{m}$. If d is known, then M_D provides the normalization of the model.

The fitting procedure minimizes a χ^2 function which fits the model described in Equation 2 to the observed SED (see Fig. 3 and Table 2). 3000 fluxes are drawn from a randomly sampled normal distribution centred on the measured values with standard deviation equal to the uncertainty in each photometry measurement. We use only the *Herschel* PACS and SPIRE photometry for the fit, since these measurements have the least contamination from emission lines.

The total dust mass resulting from this procedure is $M_D = 0.36 \pm 0.09 M_\odot$ and the characteristic dust temperature is $T_D = 37.52 \pm 6.51$ K. The emissivity index returned by the fit is $\beta = 2.02 \pm 0.38$. The obtained β value is sufficiently close to the spectral index of the underlying theoretical dust model, $\beta = 2$, suggesting that the emission for $\lambda \geq 100\mu\text{m}$ comes from dust in a very narrow temperature range, i.e., very likely a dust population with a small range of grain sizes. This MBB fit is shown in Figure 3 in comparison with the observed SED. This figure shows that the complete SED is too broad to be fit by a single population of grains. We conclude that a detailed model should include at least two populations of grains, as has been suggested from previous IR studies of WR nebulae (e.g., Mathis et al. 1992).

It is important to note that the MBB fit gives us no information on the properties of the small grains, which absorb most of the stellar radiation and are responsible for the majority of the mid-infrared emission from the nebula. Nevertheless, the value of T_D estimated in this section will be a useful guide to restrict the large grain temperature in our detailed, self-consistent photoionization model of M 1-67 (see below).

3 DETAILED MODELLING OF M 1-67

Our aim is to produce a model of M 1-67 that can simultaneously explain both the nebular optical properties and its infrared photometry and spectroscopy. For our reference optical observations, we use the high spatial resolution spectroscopic results presented by Esteban et al. (1991). We chose these observations rather than the more recent integral field spectroscopy observations of Fernández-Martín et al. (2013) because the slit positions of Esteban et al. (1991) give spectra that are more representative of average con-

ditions in the nebula. Furthermore, we assume that M 1-67 can be modeled as a purely photoionization nebula since there are no apparent signs of interaction between a fast wind and the clumpy nebula material (Fernández-Martín et al. 2013). The kinematics of the clumps suggests an ejecta origin rather than the breakup of a swept-up shell due to instabilities (Solf & Carsenty 1982; Grosdidier et al. 1998; Toalá & Arthur 2011).

The nebular material consists of gas and dust, both of which interact with the UV flux from the central star and so cannot be treated separately. The spectral synthesis and plasma simulation code CLOUDY (Ferland et al. 2017) is the ideal tool to investigate this interaction, coupled with the PYCLOUDY library (Morisset 2014) to obtain the fluxes and line intensities through apertures corresponding to the different instruments and observations we wish to model.

CLOUDY uses as input parameters: (i) the stellar properties (luminosity and spectral shape), (ii) the nebular properties (abundances and radial density profile) and (iii) dust properties (species, size distributions and dust-to-gas ratio). Calculations were performed with version 17.01 of CLOUDY, last described by Ferland et al. (2017).

3.1 Stellar atmosphere

The spectra of WN-type WR stars are the result of non-LTE radiative transfer through expanding atmospheres including line blanketing by iron and iron-group elements (Gräfener et al. 2002) and, as such, the spectral shape departs strongly from that of a black body spectrum. In particular, the absorption of UV photons drives powerful stellar winds, which have a ratio of mechanical to radiation momentum much larger than unity due to multiple scattering. Detailed synthetic spectra should be used when modelling the observable properties of WR nebulae (see Reyes-Pérez et al. 2015) and in this paper we use the Potsdam Wolf-Rayet (PoWR) model atmospheres (Hamann et al. 2006), which have been developed over many years and include effects such as line-blanketing and clumping in the wind.⁵

WR 124 was given the spectral classification WN8h on the basis of its optical spectrum (Smith & Aller 1969). Hamann et al. (2006) modelled the atmosphere of this star with the PoWR code and the best fit in R_t - T_{eff} space to the *IUE* flux and narrow-band visual photometry is model 06-14 from the WNL-H20 grid of models. Here, R_t is the transformed radius, related to the mass-loss rate \dot{M} by

$$R_t = R_* \left\{ \frac{v_\infty}{2500 \text{ km s}^{-1}} \left/ \frac{\dot{M} \sqrt{D}}{10^{-4} M_\odot \text{ yr}^{-1}} \right. \right\} \quad (4)$$

where R_* is the stellar radius, v_∞ is the stellar wind velocity and D is a clumping factor. Stellar luminosity, temperature and radius are related through the Stefan-Boltzmann law. The radius, luminosity and mass-loss rate can be scaled with distance using the transformation law Equation 4. Details of the WNL 06-14 PoWR grid model are listed in Table 3. In Figure 4 we show the comparison between the synthetic spectrum WNL 06-14 obtained with the PoWR model atmosphere code and black body radiation with the same effective temperature. The model atmosphere is extremely deficient in EUV photons compared to the black body spectrum due to photon reprocessing in the stellar wind driving region. We rescaled the luminosity of WR 124 calculated by Hamann et al. (2019) to our adopted

⁵ <http://www.astro.physik.uni-potsdam.de/~wrh/PoWR/powrgrid1.php>

Model	WNL 06-14
X_{H} [%]	20
T_{eff} [kK]	44.7
$\log_{10} R_t$ [R_\odot]	0.7
$\log_{10} \dot{Q}_{\text{H}}$ [s^{-1}]	48.85
$\log_{10} \dot{Q}_{\text{He}}$ [s^{-1}]	44.91
D_∞	4

Table 3. Parameters of PoWR Model WNL 06-14, which was found by Hamann et al. (2006) to be the best fit to the stellar spectrum of WR 124.

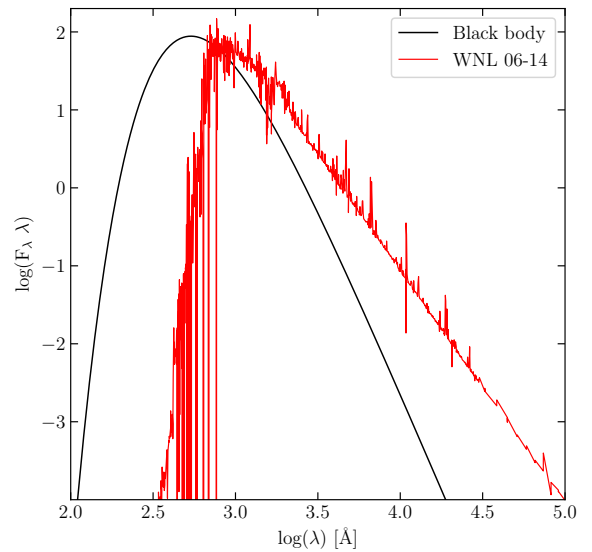


Figure 4. Comparison between black body emission and PoWR stellar atmosphere model. Solid (red) line: best-fit model to WR 124 determined by Hamann et al. (2006) corresponding to model WNL 06-14 with $T_{\text{eff}} = 44.7$ kK. The black line represents the black body spectrum with the same effective temperature.

distance of 6.4 kpc, and obtain a luminosity of $L = 10^{5.76} L_\odot$ for WR 124. The WN8 class of stars is among the most luminous stars known.

3.2 Nebular properties

In $H\alpha$ images M 1-67 has a clumpy appearance, while kinematic studies suggest it is comprised of an expanding hollow shell of clumps. Grosdidier et al. (1998) found that the radial $H\alpha$ surface-brightness distribution can be reproduced by a radial power-law density distribution of the form

$$n_e(r) = n_0 \left(\frac{r_{\text{in}}}{r} \right)^\alpha, \quad (5)$$

with power-law index $\alpha = 0.8$. Furthermore, the nebula must be density bounded with an external cutoff radius because $H\alpha$ images show that the nebula is completely ionized (Grosdidier et al. 1998). Fernández-Martín et al. (2013) report electron densities of $n_e \sim 1500 \text{ cm}^{-3}$ in the central regions of the nebula and

	Esteban et al. (1991) ¹	Fernández-Martín et al. (2013) ²
O	8.12	7.70
S	6.96	6.40
N	8.54	8.21

Table 4. Chemical abundances in M 1-67 shown in $12+\log_{10}X$ notation. ¹ Region A. ² Regions 5 and 6.

$n_e \sim 650 \text{ cm}^{-3}$ in the outer regions with a symmetric gradient. Sirianni et al. (1998) calculate the electron densities at 270 positions in M 1-67 and find densities as low as 150 cm^{-3} in external parts of the nebula and some central positions with densities as high as 2400 cm^{-3} . Vamvatira-Nakou et al. (2016) make the approximation that the nebula is a spherical shell with inner radius $r_{\text{in}} = 45 \text{ arcsec}$ (Solf & Carsenty 1982) and outer radius $r_{\text{out}} = 60 \text{ arcsec}$ (Grosdidier et al. 1998). In our models, we adopt a density distribution similar to Equation 5 and vary n_0 , r_{in} and α . We also consider multiple shells and take in to account the bipolar appearance of the dust emission evident in Figure 1.

Esteban et al. (1991) derive chemical abundances for 4 positions in M 1-67, while Fernández-Martín et al. (2013) determined abundances for 8 different regions; both studies agree that nitrogen is enriched while oxygen is deficient in the nebula as a result of processing in the CNO cycle. Their results are summarized in Table 4. We note, however, that the derived chemical abundances from these studies vary with position in M 1-67.

3.3 Dust properties

The photospheres of evolved massive stars are oxygen-rich, rather than carbon-rich, due to nucleosynthesis by the CNO cycle in the core, which favours the production of ^{14}N at the expense of ^{12}C . The dust formed in RSG and LBV should therefore be primarily calcium-magnesium-iron silicates, such as olivine (MgSiFeO_4), and metal oxides, such as alumina (Al_2O_3) (see, e.g., Gail et al. 2005; Cherchneff 2013). We examined the publicly available *Spitzer* IRS spectra to search for grain emission features but found no evidence for crystalline silicates at their known wavelengths 6, 11.3, 19, 23, 27, 33 μm (Henning 2010). Accordingly, we assume the grains are composed of amorphous astronomical silicate material (Greenberg & Li 1996), specifically olivine (MgFeSiO_4), which is the default silicate grain option in CLOUDY.

The grains are spherical and are resolved into size bins described by a power-law distribution $N(a) \propto a^{-3.5}$ (MRN size distribution; Mathis et al. 1977), with typically 10 size bins between a_{min} and a_{max} where the minimum and maximum grain sizes are free parameters. The dust-to-gas mass ratio (D/G) in CLOUDY can be adjusted by the user but the default value defines the Si abundance in the silicate dust to be 3.28×10^{-5} , equivalent to the Solar value, and the mass number per dust molecule is 172 (e.g., Weingartner & Draine 2001).

3.4 Synthetic spectra and photometry

For a given set of input parameters, CLOUDY calculates the ionization and thermal equilibrium solution and computes the continuum and line volume emissivities as a function of radius and depth for the full spectral range from X-rays to radio wavelengths. We used

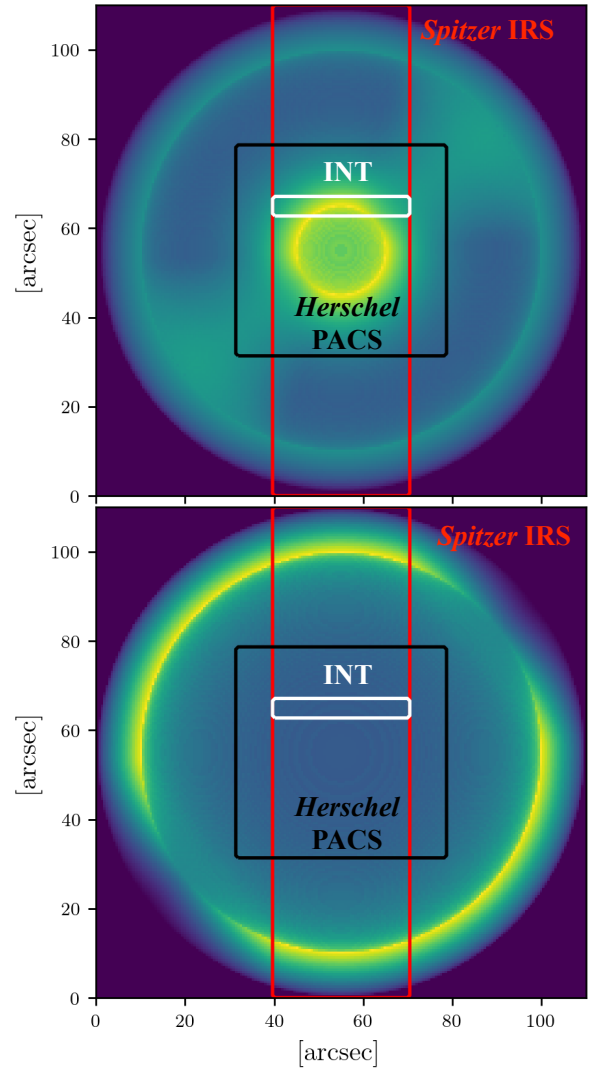


Figure 5. Synthetic emission maps obtained from our best model MC 6-14 calculated by *pyCLOUDY*. Top panel: $\text{H}\beta$ emissivity on a logarithmic scale. Bottom panel: *Herschel* PACS $70 \mu\text{m}$. The rectangular regions show the relative positions and sizes of apertures representing region A of the INT slit from Esteban et al. (1991) (white), footprint of the *Herschel*-PACS spectrometer (blue), and the slit of *Spitzer* IRS observations (red).

the *pyCLOUDY* library (see Morisset 2006) to produce surface brightness maps from the spherically symmetric emissivity results of our models. We extracted simulated optical spectra from a synthetic aperture with the same angular size and position as slit A of the Isaac Newton Telescope (INT) observations presented by Esteban et al. (1991) (see Figure 5).

We also simulated the broadband infrared photometry corresponding to the *WISE*, *Spitzer* and *Herschel* observations shown in Figure 1 and Table 2. The continuum emission is integrated over each photometer band weighted by the corresponding transmission curve⁶.

⁶ <http://svo2.cab.inta-csic.es/theory/fps/index.php?mode=browse>

Parameter	MA 6-14	MB 6-14		MC 6-14			
		Inner shell	Outer shell	Inner Shell		Outer Shell	
				Zone 1	Zone 2	Zone 3	Zone 4
Distance [kpc]	6.4	6.4	6.4	6.4	6.4	6.4	6.4
$\log_{10}(L_{\star}/L_{\odot})$	5.76	5.76	5.76	5.76	5.76	5.76	5.76
$c(\text{H}\beta)$	1.9	1.9	1.9	1.9	1.9	1.9	1.9
Inner radius["]	10	10	45	10	10	45	45
Outer radius["]	55	45	55	45	45	55	55
n_0 [cm ⁻³]	2100	2500	600	2500	900	600	666
α	1.4	2.0	2.0	2.0	0.2	2.0	2.0
Filling Factor	0.05	0.05	0.037	0.05	0.02	0.0365	0.005
a_{small} [μm]	0.005–0.25 ^(a)	-	0.005–0.05 ^(a)	-	-	0.005–0.05 ^(a)	-
a_{big} [μm]	-	-	0.9 ^(b)	-	-	0.9 ^(b)	-
B/S	-	-	20	-	-	20	-
D/G	4.03×10^{-3}	-	3.87×10^{-2}	-	-	6.33×10^{-2}	-
Gas mass [M_{\odot}]	11.87	5.48	5.78	3.29	2.19	3.41	0.35
Dust mass [M_{\odot}]	0.05	-	0.22	-	-	0.22	-

Table 5. Input parameters for the model sets discussed in the text. ^(a) Population of grains with a standard MRN grain size distribution. ^(b) Population of grains represented by a single size.

3.5 Constraints on the models

In order to assess if a model is a good fit to the observations, we need to define some constraints. We selected the following:

- (i) the total observed $\text{H}\alpha$ nebular flux. This was taken from Grosdidier et al. (1998);
- (ii) the $\text{H}\beta$ surface brightness $F(\text{H}\beta)$ obtained from the INT slit A aperture taken from Esteban et al. (1991);
- (iii) the gas electron temperature T_e derived from the $[\text{N II}]\lambda\lambda 5755/6584$ ratio from the INT slit A aperture taken from Esteban et al. (1991);
- (iv) the shape and flux of the IR photometry obtained from all images shown in Figure 1, illustrated in Figure 3 and listed in Table 2.

We do not attempt to fine-tune the chemical abundances of our models and we keep them fixed at the values reported by Esteban et al. (1991). This may lead to differences between observed and model emission-line intensities for some elements, but line ratios should not be affected. We note that derived conditions across M 1-67 are not uniform due to the clumpiness of the nebula (Esteban et al. 1991; Fernández-Martín et al. 2013), but we do not model discrete clumps in the present work.

4 RESULTS

In this section, we describe the results of a series of models varying the density distribution and the dust properties, leading to a self-consistent description of the nebular optical and IR properties of M 1-67.

4.1 Gas Density Distribution

We begin by investigating the gas density distribution. We ran a set of CLOUDY models using the PoWR 06-14 stellar atmosphere model (Hamann et al. 2006) as input and including pure silicate grains with an MRN power-law size distribution represented by

Instrument	Parameter	Observations	MA 6-14	MB 6-14	MC 6-14
<i>HST</i> ^(a)	$\log_{10}F(\text{H}\alpha)$	-10.55 ⁽¹⁾	-10.56	-10.55	-10.55
INT ^(b)	$\log_{10}F(\text{H}\beta)$	-13.01 ⁽²⁾	-13.03	-13.07	-13.105

Table 6. Emission lines used to constrain our models: ^(a) Total $\text{H}\alpha$ flux, ^(b) $\text{H}\beta$ surface brightness through INT slit A. The errors from the observational measurements are statistical, of order $\sim 5\%$. ⁽¹⁾ Grosdidier et al. (1998). ⁽²⁾ Esteban et al. (1991).

10 size bins in the range $0.005\mu\text{m}$ to $0.25\mu\text{m}$, which is the standard ISM size distribution. We fixed the outer radius of the nebula, $r_{\text{out}} = 55$ arcsec (Grosdidier et al. 1998) and allowed the inner radius r_{in} to vary. The density in the shell obeys a power-law distribution given by Equation 5, where the power-law index and the density at the inner radius are to be determined and we assume spherical symmetry. Using the constraints of the observed total $F(\text{H}\alpha)$ flux and the $F(\text{H}\beta)$ surface brightness and the electron temperature T_e , we varied the inner radius r_{in} , the density at the inner radius n_0 and the power-law index α until the model estimates of the observed constraint parameters agreed within 25% for each value. The best model, labeled as MA 6-14, resulted from the parameter values $n_0 = 2100\text{ cm}^{-3}$ and $\alpha = 1.4$, with inner and outer radii of 10 and 55 arcsec, respectively.

Input details of model MA 6-14 are listed in column 2 of Table 5. The output values of the constraint parameters for this model are given in Table 6. Additionally, in Table 7, model predicted emission-line intensities are compared to observed values at optical and IR wavelengths from different apertures. We note that although the low-ionization lines of ions such as $[\text{N II}]$ are well reproduced by the model, higher ionization lines, for example, $[\text{S III}]$ are not well-modeled. We attribute this to the stellar atmosphere model, which lacks photons capable of photoionizing S to S^{++} . We also note that this model produces a reasonable amount of emission in the $[\text{C II}]\lambda 158\mu\text{m}$ line. Vamvatira-Nakou et al. (2016) interpreted this emission as being produced in a photon-dominated region (PDR) but our models are fully ionized and density bounded.

Instrument	Line	Observed	MA 6-14	MB 6-14	MC 6-14
INT ⁽¹⁾	H β	100.0	100.0	100.0	100.0
	H α	296.0	298.4	298.3	298.2
	[N II] 5755	0.9	0.7	0.8	0.8
	[N II] 6584	314.0	287.8	291.6	294.9
	[N II] 6548	108.0	97.6	98.9	100.0
	[O II] 3727	15.0	15.3	15.4	15.8
	[S II] 6716	13.2	17.6	17.1	17.5
	[S II] 6731	16.2	21.1	20.9	21.2
	[S III] 9068	12.0	3.5	3.7	3.7
	[S III] 9530	30.6	8.9	9.3	9.3
	$F(\text{H}\beta) \times 10^{-14}$	9.81	9.43	8.44	7.86
Spitzer	$T_e[\text{N II}]5755/6584$	6019	5866	5894	5909
	$n_e[\text{S II}]6716/6731$	947	885	925	898
	H I 12.3 μm	5.2	5.2	5.2	5.2
	[Ne II] 12.81 μm	165.9	139.2	137.9	139.1
IRS	[Ne III] 15.5 μm	3.1	0.0	0.0	0.0
	[S III] 18.7 μm	251.5	47.8	46.0	45.9
	[S III] 33.5 μm	263.8	37.3	35.6	35.9
	$n_e[\text{S III}]18.7/33.5$	554	922	936	922
		[W/m ²]	[W/m ²]	[W/m ²]	[W/m ²]
Herschel PACS ⁽²⁾	[N II] 121 μm	13.1	18.5	15.0	14.7
	[N II] 205 μm	1.9	2.6	2.2	2.1
	[N III] 57.2 μm	0.3	0.0	0.0	0.0
	[O I] 63.2 μm	1.3	0.0	0.0	0.0
	[O I] 145 μm	0.1	0.0	0.0	0.0
	[C II] 158 μm	2.1	5.3	4.3	4.3

Table 7. Emission lines considered in our models. Optical lines are relative to H β = 100 and infrared line measurements obtained from IRS spectra using the PAHFIT IDL routine (Smith et al. 2007) are relative to H I 12.3 μm . The errors from the observational measurements are statistical, of order ~ 5%. ⁽¹⁾ Esteban et al. (1991). ⁽²⁾ Vamvatira-Nakou et al. (2016).

The simple model described above reproduces the gas low-ionization emission reasonably well. However, the thermal dust emission resulting from the ISM size distribution of silicate grains that are homogeneously mixed with the gas at all radii leads to the SED shown in Appendix B (see Figure B1). There is a clear excess of emission at shorter wavelengths, i.e., there is too much hot dust.

The dust temperature can be lowered by either increasing the size of the dust grains or moving the dust further away from the star. To better understand the distribution of dust in the nebula, we calculated the radial distribution of the surface brightness of the 70 μm emission integrated over the bipolar shape seen in Figure 1. This has been done by using the CART2POL routine⁷. The radial distribution of the 70 μm emission shown in Figure 6 strongly suggests that it originated in a shell. Furthermore, the radial distribution of the H α surface brightness for the same bipolar region shows evidence for emission from a structure at intermediate radii (see Figure 6).

The MBB fit to the long-wavelength ($\lambda \geq 100 \mu\text{m}$) *Herschel* emission suggested that the grains responsible for this part of the SED have a characteristic temperature of $T_D = 38 \text{ K}$. This grain population will represent the bulk of the mass of grain material in the nebula and will be comprised of large grains. On the other hand, small grains are necessary to produce the short wavelength thermal

emission, and these grains absorb a greater proportion of the UV photons and affect the optical properties of the nebula.

4.2 Dust models

4.2.1 Two-shells model

Our second scenario proposes that M 1-67 is composed of an inner shell with no contribution from dust and an outer shell with gas and two populations of grains (see e.g. Gómez-Llanos et al. 2018). The inner dust-free shell is delimited by r_{in} and r_{mid} , whilst the outer shell material is distributed between r_{mid} and r_{out} . The region interior to r_{in} is empty.

We begin by setting r_{mid} to 45 arcsec, which corresponds to the radius of the ring of expanding clumps reported by Solf & Carsenty (1982) and Sirianni et al. (1998), and fix the outer radius at $r_{\text{out}} = 55 \text{ arcsec}$, as before. The other parameters, that is, r_{in} , the power-law index in both shells ($\alpha_{\text{in}}, \alpha_{\text{out}}$), the density normalizations ($n_{0,r_{\text{in}}}, n_{0,r_{\text{mid}}}$) and the filling factors ($f_{\text{in}}, f_{\text{out}}$) were arrived at during an exhaustive process of testing different dust grain size distributions and dust-to-gas ratios in the outer shell while adjusting the inner shell parameters to maintain compliance with the observational constraints listed in § 3.5. We found that the total H α flux is most sensitive to the outer shell parameters, since that is where the bulk of the nebular mass resides, while the H β surface brightness is most affected by the density distribution near r_{in} where the INT aperture is located.

Our best spherically symmetric two-shell model, labeled MB 6-14, comprises two concentric shells: the inner, dust-free shell is delimited by $r_{\text{in}} = 10 \text{ arcsec}$ and $r_{\text{mid}} = 45 \text{ arcsec}$, has power-law index $\alpha = 2$, density normalization $n_{0,r_{\text{in}}} = 2500 \text{ cm}^{-3}$ and filling factor $f_{\text{in}} = 0.05$, and the outer, dusty shell is bounded by $r_{\text{mid}} = 45 \text{ arcsec}$, $r_{\text{out}} = 55 \text{ arcsec}$, has power-law index $\alpha = 2$, density normalization $n_{0,r_{\text{mid}}} = 600 \text{ cm}^{-3}$ and a smaller filling factor, $f_{\text{out}} = 0.037$. The dust properties that give a good fit to the observed IR SED combine a population of large grains of representative size 0.9 μm (‘big grains’) and a population with a MRN power-law size distribution between 0.005 μm and 0.05 μm (‘small grains’), with a much higher proportion of big grains than small grains. It was also necessary to increase the dust-to-gas ratio above the default value in the outer shell. Details of this model are listed in the third and fourth columns of Table 5.

Model MB 6-14 does a good job of fitting the nebular optical and IR emission lines as well as reproducing T_e and n_e (see Table 6 and 7). The total ionized gas mass resulting from this model is 11.26 M_\odot and the dust mass is $M_D = 0.22 M_\odot$.

We found that dust with sizes between 0.8–1.0 μm (represented, for simplicity, by a population of single-size grains of size 0.9 μm), and located in the outer shell, has a very similar temperature to the characteristic dust temperature suggested by the MBB fit, that is $T_D \sim 38 \text{ K}$. The shorter wavelength part of the IR SED requires a population of smaller grains with sizes in the broad range 0.005 μm to 0.05 μm . The dust in the smallest size bin is twice as hot.

4.2.2 Bipolar shells model

Motivated by the evident bipolar morphology revealed by the IR images (see Fig. 1), we introduced a further refinement to our models. PYCLOUDY enables us to use fully 3-dimensional density structures and so we relaxed our assumption of spherical symmetry and defined the bipolar density distribution depicted in Figure 7. The

⁷ <https://github.com/e-champenois/cart2pol>

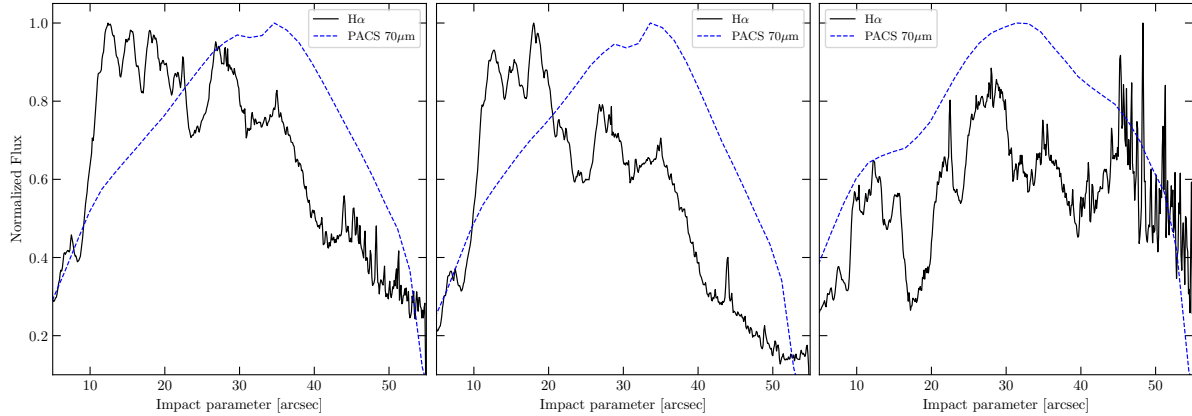


Figure 6. Projected radial distribution of the surface brightness integrated over (a) whole nebula ($0^\circ \leq \phi \leq 360^\circ$), (b) the bipolar emission region of M 1-67 at $70\mu\text{m}$ ($-30^\circ \leq \phi \leq 90^\circ$ and $130^\circ \leq \phi \leq 230^\circ$), and (c) regions outside of bipolar emission ($90^\circ \leq \phi \leq 130^\circ$ and $230^\circ \leq \phi \leq 330^\circ$). The solid black line is the observed $\text{H}\alpha$ surface brightness. The dashed blue line is the observed surface brightness from the *Herschel* PACS band at $70\mu\text{m}$.

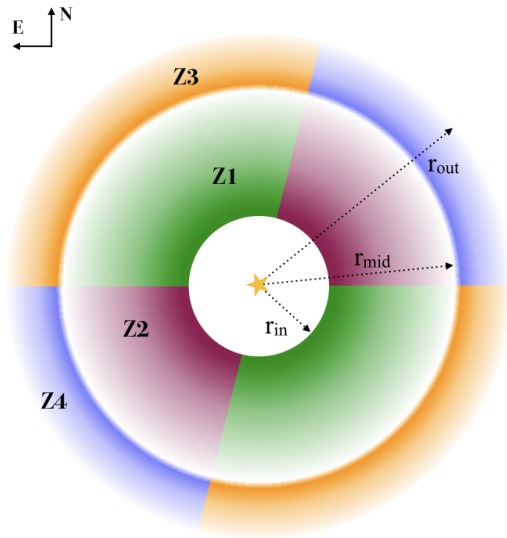


Figure 7. Schematic view of the distribution of gas and dust in M 1-67. Regions Z1 (green) and Z2 (purple) are composed purely of gas but with differing density distributions; region Z4 (blue) is also dust free and has a steeper power law to Z2; Z3 (orange) is the only region that contains dust, see Table 5 for details of the density distributions. The white region interior to r_{in} is completely empty of both gas and dust. The diagram depicts a vertical slice ($y = 0$ plane) of the 3D model, which must be rotated through $\phi = \pi$ and oriented with respect to the observer in order to produce the emission maps.

form of the density law in the different regions of the bipolar structure was guided by the surface brightness profiles depicted in panels (b) and (c) of Figure 6.

The final model, labeled MC 6-14, consistent with both the optical constraints detailed in § 3.5 and the observed IR SED, is similar to the previous model MB 6-14 in that it requires an inner, dust-free shell and an outer shell where the dust resides. However, in addition, both the inner and outer shells are divided into sectors having different density distributions and, moreover, part of

the outer shell is dust free, to simulate the bipolar nature of the dust emission seen in the IR images.

In Figure 7 regions Z1 (green) and Z2 (purple) are dust-free inner regions, region Z4 (blue) is a dust-free outer region, and region Z3 (orange) is the only region that contains dust. The density distribution in region Z1 is a steep power law, while that in region Z2 is much flatter, as suggested by the surface brightness profiles in Figure 6. The outer regions, Z3 and Z4, both require a steep fall-off in density but the filling factor in the dust-free sector is much lower than that in the dusty region. Full details of the parameters for this model are given in Table 5. In addition, we must specify the viewing angle and the placement of the apertures for the INT and PACS simulated emission lines. In particular, the INT aperture crosses regions Z1 and Z2, illustrated in Figure 5.

The simulated radial $\text{H}\alpha$ surface brightness distribution of this model is shown in Figure 8. The dust properties that give a good fit to the observed IR SED combine a population of large grains of representative size $0.9\mu\text{m}$ (‘big grains’) and a population with a MRN power-law size distribution between $0.005\mu\text{m}$ and $0.05\mu\text{m}$ (‘small grains’). As expected, these are the same populations as we found for the two shells model discussed above and we find the same proportion of big to small grains. However, now that all the dust is confined to a smaller volume of the model, we require an even higher dust-to-gas ratio to explain the observations (see Table 5). The resultant temperature profiles for the different grains in our model are shown in Figure 9. Variations in temperature across the shell are small for a given dust size bin but there are noticeable temperature differences between small grains and large grains.

The synthetic $70\mu\text{m}$ radial surface brightness distribution corresponding to these grain distributions is shown in Figure 8. Details of the optical and infrared emission lines of this model are presented in Table 6 labeled as MC 6-14. The synthetic SED obtained from MB 6-14 is shown in Figure 3 where it can be seen to compare very well with the observed SED. In this figure we also show separately the contribution from the ionized gas and that from the dust. It can be appreciated that the major contribution of the gas is around $12\mu\text{m}$ and at $160\mu\text{m}$. The latter due to the presence of the $[\text{N II}]$ $121\mu\text{m}$ emission line (see Table 7). The free-free emission from the gas also influences the total emission at the longest wavelength point at $500\mu\text{m}$.

We note that in order to fit the IR SED we had to increase

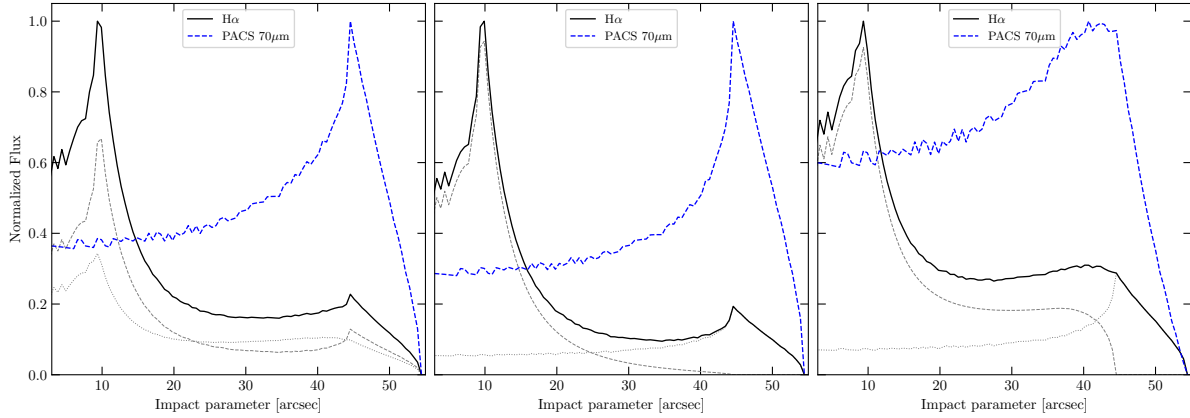


Figure 8. Projected radial distribution of the surface brightness from our best model (MC 6-14) integrated over (a) whole nebula ($0^\circ \leq \phi \leq 360^\circ$), (b) the bipolar emission region of M1-67 at $70\mu\text{m}$ ($-30^\circ \leq \phi \leq 90^\circ$ and $130^\circ \leq \phi \leq 230^\circ$), and (c) regions outside of bipolar emission ($90^\circ \leq \phi \leq 130^\circ$ and $230^\circ \leq \phi \leq 330^\circ$). The solid black line is the observed $H\alpha$ surface brightness. Right panel: The dashed gray line and the dotted gray line show Zone 2+Zone 4 and Zone 1+Zone 3 contributions, respectively. Central and left panels: The dashed gray line and the dotted gray line show inner and outer zones contributions, respectively. The dashed blue line is the observed surface brightness from the *Herschel* PACS band at $70\mu\text{m}$.

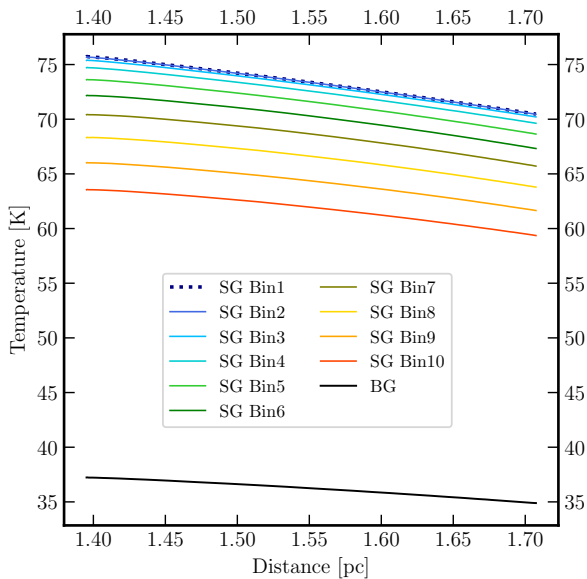


Figure 9. Dust temperature profiles from our best model MC 6-14. The model has 10 size bins from the population of small grains (SG) and only one of the big grains population (BG).

the dust-to-gas ratio in the outer shell (D/G) compared with that in the ISM (D/G_{ISM}). Our best model, MC 6-14, requires a dust-to-gas ratio 16 times that of the ISM and a mass ratio of big to small grains of $B/S = 20$. With these values, our best, self-consistent photoionization model finds a dust mass of $0.22 M_\odot$, with 95% corresponding to the big grains, and an ionized gas mass for M1-67 of $9.2^{+1.6}_{-1.5} M_\odot$. Here, the errors in the estimated ionized mass were computed taking into account the errors in the $H\alpha$ flux reported by Grosdidier et al. (1998).

5 DISCUSSION

Our best *pyCLOUDY* model successfully reproduces the IR photometry corresponding to the thermal emission from the dust in the nebula and approximates the main characteristics of the photoionized gas in M1-67. In this section we discuss the limits of our model in accounting for all of the observed spectral features, and also place our model in the context of the evolution of the central star.

5.1 Gas emission lines

The gas in the nebula absorbs the majority of the ionizing photons emitted by the star, which correspond to wavelengths around the peak of the SED. The shape of the incident stellar spectrum is important: even though WNL stars have high effective temperatures, $T_{\text{eff}} \sim 45$ kK, the EUV photons are reprocessed to longer wavelengths in the process of driving the strong stellar wind. The stellar spectrum that emerges is lacking in the highest energy photons, $h\nu > 25$ eV (see Figure 4 and Table 3). Thus, the electron temperature in the nebular gas is low, $T_e \sim 5909$ K and high ionization lines, such as $[\text{O III}] \lambda 5007$, are absent.

In M1-67, the observed low-ionization emission features of hydrogen, nitrogen and sulphur in the optical spectra are consistent with the photoionization of an essentially power-law density distribution (see, e.g., Eq. 5) by the WNL stellar spectrum proposed by Hamann et al. (2006), with the chemical abundances derived by Esteban et al. (1991). Our best model returns derived electron temperatures and densities from simulated emission-line ratios (see Table 7) within the ranges reported in the literature (e.g., Esteban et al. 1991; Fernández-Martín et al. 2013; Sirianni et al. 1998). However, our models are not able to reproduce the intensities of high-ionization species, such as $[\text{S III}]$, which are seen in optical and *Spitzer* IRS spectra. Furthermore, the emission of the neutral $[\text{O I}] 63\mu\text{m}$ line detected in selected *Herschel* PACS spatial pixels (Vamvatira-Nakou et al. 2016) is not replicated by our models.

Although our best model does produce some $[\text{S III}]$ emission, the simulated intensities of the optical $\lambda\lambda 9068 \text{ \AA}$ and 9530 \AA lines and the IR $18.7\mu\text{m}$ and $33.5\mu\text{m}$ lines are much lower than what is observed in M1-67. In addition, our *CLOUDY* models do not pro-

duce any [Ne III] or [N III] emission, which is seen in the *Spitzer* IRS and *Herschel* PACS spectra, respectively. In our photoionization model, the [S III] emission is produced primarily at the inner radius r_{in} by the most energetic photons of the incident stellar spectrum. It is not possible to model these high-ionization species with the adopted stellar SED (WNL 6-14), which Hamann et al. (2006) found to be a good fit to the optical and UV spectra of WR 124. An SED with a greater proportion of photons able to photoionize S to S^{++} may be required. Alternatively, we speculate that the high-ionization emission lines could be produced in shocks but such physics is not included in CLOUDY. For example, shocks could form in the 88 km s^{-1} bipolar flow detected by Sirianni et al. (1998) and Fernández-Martín et al. (2013), which is oriented in a northwest-southeast direction. Alternatively, the [S III] emission could arise close to the star where the fast stellar wind shocks against the innermost nebular material.

The other emission lines that our photoionization model does not reproduce are those of neutral oxygen. Although Esteban et al. (1991) only find upper limits for the optical [O I] $\lambda 6300 \text{ Å}$ line, in the infrared the [O I] $63 \mu\text{m}$ is detected in several of the *Herschel* PACS spaxels, and is strongest for those that cover bright regions of emission at $70 \mu\text{m}$. The $63 \mu\text{m}$ line is usually emitted by neutral gas in the PDR just outside an ionization front. We speculate that this emission comes from small, dense, unresolved neutral clumps in the nebula, which are photoionized on their surface closest to the central star. The [O I] $\lambda 6300 \text{ Å}$ optical line emission that we would expect to see from the ionization front is simply too weak to detect from such small regions. In addition, we have inspected both the $\text{H}\alpha$ image of Grosdidier et al. (1998), and the emission-line maps presented by Fernández-Martín et al. (2013) and we do not see the characteristic photoevaporated flows coming off the starward side of the condensations in the nebula that we might expect if the neutral material is the main component of the condensations we see coincident with the PACS spaxels superimposed on the $70 \mu\text{m}$ image. Fernández-Martín et al. (2013) do find that the reddening coefficient $c(\text{H}\beta)$ is not homogeneous across the nebula, and varies between 1.3 and 2.5. There is no particularly extreme value associated with any of the blobs in the $70 \mu\text{m}$ image.

5.2 Dust properties

The dust size distribution predicted by our models consists of two populations: the first has a MRN power-law size distribution with $a_{\text{min}} = 0.005 \mu\text{m}$ and $a_{\text{max}} = 0.05 \mu\text{m}$ and a power-law index $q = -3.5$. The second population consists of large grains with representative size $a_{\text{big}} = 0.9 \mu\text{m}$, which are necessary to reproduce the $\lambda \geq 100 \mu\text{m}$ *Herschel* photometry. We find that a mass proportion between big grains and small grains of $B/S = 20$ is required. The maximum size of the grains is considerably smaller than that predicted by Vamvatira-Nakou et al. (2016), whose pure dust model required a population of large dust grains up to $10 \mu\text{m}$ in size to model the *Herschel* photometric observations. In our models, the gas absorbs and processes most of the ionizing photons, so it is not necessary to have such large dust grains to reproduce the dust temperature indicated by the photometry (see § 4.2). A maximum grain size $a_{\text{big}} = 0.9 \mu\text{m}$ is much easier to explain than $10 \mu\text{m}$. Kochanek (2011) showed that dust formation in the winds of evolved massive stars $M_{\text{ZAMS}} \geq 40 M_{\odot}$ most likely occurs through eruptive events in an LBV phase, such as the “great eruption” of η Carina. This is because the mass-loss rate \dot{M} needs to be high enough to shield the dust-formation region from soft UV photons. Mass-loss rates $\dot{M} \geq 10^{-2} M_{\odot} \text{ yr}^{-1}$ are required to obtain $a_{\text{big}} > 1 \mu\text{m}$. The maxi-

mum grain size of our best-fit model is $a_1 = 0.9 \mu\text{m}$, which requires mass-loss rates above $\dot{M} > 10^{-3} M_{\odot} \text{ yr}^{-1}$ (see fig. 2 of Kochanek 2011). An eruptive scenario would be consistent with the kinematic evidence of M 1-67 presented by Sirianni et al. (1998), which consists of a hollow shell of clumps expanding at 46 km s^{-1} centred on WR 124. The second N-rich bipolar kinematic component with expansion velocity $\sim 88 \text{ km s}^{-1}$ (Sirianni et al. 1998; St-Louis et al. 2017) is not spatially coincident with the dust emission shown in our Figure 1.

Our estimate for the total mass of dust in M 1-67 is $M_{\text{D}} = 0.22 M_{\odot}$, of which $0.206 M_{\odot}$ corresponds to the largest size grains, $a_{\text{big}} = 0.9 \mu\text{m}$. This is $\sim 2/3$ smaller than the dust mass obtained from the modified black body model (see § 4.2), and suggests that the standard Milky Way normalization $\kappa_{\text{r}0}$ value is not appropriate for M 1-67. Indeed, the normalization value $\kappa_{\text{r}0}$ includes the standard Milky Way hydrogen-to-dust ratio, set to $H/D = 90$ (Draine 2003; Bianchi et al. 2019), but we have found that a much higher proportion of dust is required in this nebula.

Increasing the mass of silicate grains by a factor of sixteen as required by our model is puzzling and needs some further discussion, since the underlying assumption was that virtually all of the available silicon atoms were locked up in dust grains (Weingartner & Draine 2001). Thus, to increase the mass fraction we would require more silicon atoms than are available. A possible explanation is a nucleosynthesis event such as that proposed by Podsiadlowski et al. (2010) through an explosive common envelope ejection (ECEE) scenario but we calculate that the energy liberated in fusion reactions to produce the atoms needed for the extra silicate dust grains is $9.7 \times 10^{-7} \text{ erg nucleon}^{-1}$. That is, the energy to convert $0.22 M_{\odot}$ into dust is $2.50 \times 10^{50} \text{ erg}$. This amount of energy would result in the surrounding envelope being expelled at velocities far higher than the 46 km s^{-1} expansion velocity observed in the shell. This scenario is therefore unlikely.

A more viable explanation is that the silicate grains have different optical properties to the spherical grains assumed in our models. For example, Siebenmorgen et al. (2014) find that spheroidal grains have far-IR absorption cross-sections a factor 1.5–3 larger than spherical grains with the same volume. Dust masses estimated without taking this into account would be overestimated by the same factor. Additionally, Gómez-Llanos et al. (2018) found that the emission of spheroidal grains is shifted to longer wavelengths in comparison with spherical grains. If the grains are fluffy, that is, porous aggregates of smaller grains, the absorption cross-sections will be even higher and a much smaller mass of grain material would be required to reproduce the observed IR SED. We intend to explore different grain properties in future work.

5.3 Mass loss and stellar evolution

Our PYCLOUDY model MC 6-14 finds the ionized gas mass in the nebula to be $9.2_{-1.5}^{+1.6} M_{\odot}$. The estimated mass for the central star WR 124 is $22 M_{\odot}$ (Hamann et al. 2019), which means that the initial mass for this star was at least $31 M_{\odot}$. If we take into account mass loss during main sequence evolution where single stars with ZAMS masses above $30 M_{\odot}$ can lose $\sim 10 M_{\odot}$ (see Ekström et al. 2012; Georgy et al. 2012), the initial mass for WR 124 could easily be $> 40 M_{\odot}$.

We can estimate the average mass-loss rate of the star during the dust-formation stage. Assuming a constant expansion velocity of 46 km s^{-1} , the elapsed time between the ejection of the outer ($r_{\text{out}} = 55 \text{ arcsec}$) and inner ($r_{\text{in}} = 45 \text{ arcsec}$) edges of the shell is

6.6×10^3 yrs, where we have taken the distance to the nebula to be 6.4 kpc. According to our model, the mass of gas corresponding to the shell is $3.98 M_{\odot}$, then the mass-loss rate when the shell was expelled is of order $\dot{M}_{\text{shell}} = 6 \times 10^{-4} M_{\odot} \text{yr}^{-1}$. This is within the range of values listed for mass-loss rates of known Galactic LBVs with dusty shells (see Table 1 in Kochanek 2011).

We have discussed WR 124 and its surrounding nebula in the context of single massive star evolution. *Hipparcos* light curves over the three year period 1990 to 1993 show no evidence of periodic variability so any binary companion would have to be very low mass. However, Toalá et al. (2018) recently speculated that the marginal detection of hard X-rays from WR 124 does not rule out the presence of a compact object such as a neutron star embedded within the dense stellar wind of the WN8 star. That means that the evolutionary scenario for WR 124 would include substantial mass transfer at some point (De Donder et al. 1997).

In a close binary system, common envelope evolution can lead to the ejection of the common envelope (CE), and produce a tighter binary (Ivanova et al. 2013, and references therein). Once the CE forms, frictional drag causes the secondary component of the binary to spiral-in and orbital energy is transferred to the envelope. If enough energy is transferred, a substantial fraction of the envelope can be ejected. If the gas in the envelope can recombine and form molecules during the ejection event, the recombination energy can be an additional driving mechanism for the envelope ejection (Ivanova et al. 2013). If we identify the shell between 45 arcsec and 55 arcsec in our model with the observed clumpy ring expanding at 46 km s^{-1} (Solf & Carsenty 1982; Sirianni et al. 1998), then the kinetic energy of the shell is of order 8×10^{46} erg, which is similar to that estimated for outbursts in recent optical transient events that have been associated with mass-transfer processes in binary systems (Kashi & Soker 2010). Such accretion processes can also power the ejection of a CE. However, we estimate the timescale for the ejection event in M1-67 to be much longer than, for example, the Great Eruption of the massive binary system Eta Carinae, which occurred over a twenty year period in the mid 19th century. This suggests that the spiral-in scenario is more likely, since this can occur over many dynamical timescales (Ivanova et al. 2013). Iaconi et al. (2019) have modelled the asymptotic behavior of the common envelope expansion after the end of the dynamic in-spiral, and find that it evolves into an ordered, shell-like structure at late times.

Finally, the ejecta of CE systems have been shown to be an ideal environment for dust formation, which can form more efficiently in certain CE conditions than in the envelopes of cool stars (Lü et al. 2013). The bipolar distribution of the thermal dust emission in M 1-67 at all wavelengths further supports a binary system origin. A CE phase is now thought to be one of the main routes to producing Type Ib supernovae, where the progenitors lose their hydrogen envelopes and become Wolf-Rayet stars before exploding some 10^4 – 10^6 years later, depending on the stage of evolution where the mass transfer occurs (Podsiadlowski et al. 1992).

The analysis of the IR data in combination with a self-consistent photoionization model, able to reproduce both the dust and nebular properties of M 1-67, lead us to conclude that this WR nebula has not formed by the classic wind-wind interaction scenario nor an eruptive LBV channel characteristic of single massive star evolution. We suggest that M 1-67 has formed as the result of the ejection of a CE of a binary system. If this is true, this would make M 1-67 and its progenitor star, WR 124, the first direct evidence of the post-CE scenario in massive stars.

6 SUMMARY

We have produced a self-consistent photoionization model that fits IR photometry and spectra from *WISE*, *Spitzer* (IRS and MIPS) and *Herschel* (PACS and SPIRE) of M 1-67, the nebula around WR 124. The *CLOUDY* photoionization code that we used allowed us to test different gas density distributions and dust grain size distributions. The *PyCLOUDY* tool enabled us to simulate the line emission and dust photometry through synthetic apertures corresponding to the different reference observations. Our principal findings are:

(i) The stellar atmosphere model 06-14 of the PoWR WNL grid that Hamann et al. (2006) found to be a good fit to the stellar spectrum of the central star, WR 124, is broadly consistent with the nebular optical and IR emission lines in our best model but underpredicts the intensities of high-ionization lines (see § 5.1).

(ii) We require a two-shell structure in order to model the gas and dust emission. The inner region contains only gas, and is required to reproduce the $H\alpha$ surface brightness distribution and total emission. The outer shell contains both dust and gas and is needed to reproduce the $70\mu\text{m}$ surface brightness profile and the dust temperature. The outer shell could correspond to the clumpy ring at 45 arcsec radius, which expands at 46 km s^{-1} . Both inner and outer shells have a power-law distribution of material (see § 4.2.1).

(iii) The dust grain size distribution resulting from our photoionization model consists of two populations of pure silicate grains. The first is a MRN power law with $a_{\text{min}} = 0.005 \mu\text{m}$, $a_{\text{max}} = 0.05 \mu\text{m}$ and power-law index $q = -3.5$. The second is a population of large grains with representative size $a_{\text{big}} = 0.9 \mu\text{m}$, where the mass proportion between the big and small grain populations is $B/S = 20$. This is in stark contrast to the results of Vamvatira-Nakou et al. (2016) who required much larger grains in their dust-only radiative transfer models and highlights the role played by the nebular gas in the absorption of UV photons from hot stars (see § 5.2).

(iv) We need a silicate grain mass fraction 16 times higher than that of standard ISM dust in order to reach the flux of the infrared photometry. We suggest that non-spherical grains, whose absorption cross sections are factors of 2 or more higher than spherical grains of identical volume, could explain the discrepancy in the mass of dust and the chemical abundances of the grain materials (see § 5.2).

(v) The total dust mass in the nebula resulting from our photoionization model ($M_D = 0.22 M_{\odot}$) and the dust mass resulting from fitting a modified black body model to the *Herschel* PACS and SPIRE photometry ($M_D = 0.36 M_{\odot}$) can be reconciled if the normalization parameter $k_{\nu,0}$ takes into account the specific characteristics of the material in this WR nebula.

(vi) The maximum grain size $a_{\text{big}} = 0.9 \mu\text{m}$ and the average mass-loss rate in the shell ejection $\dot{M} \sim 6 \times 10^{-4} M_{\odot} \text{yr}^{-1}$ support an eruptive formation of M 1-67.

(vii) The estimated mass of photoionized gas in the nebula is $9.2^{+1.6}_{-1.5} M_{\odot}$. Since M 1-67 is located high above the Galactic plane ($z \sim 370 \text{ pc}$), we can assume that the nebula consists almost entirely of material ejected from the central star, WR 124. Assuming that the current mass of WR 124 is $22 M_{\odot}$ (Hamann et al. 2019) we estimate that its initial mass has to be $> 40 M_{\odot}$.

(viii) We propose that M 1-67 has been formed as a result of a common envelope ejection scenario, which easily explains the energetics and dust formation in the outer, dusty shell. This would make M 1-67 and its progenitor star (WR 124) the first observational evidence of the post-common envelope evolution in massive stars.

ACKNOWLEDGEMENTS

The authors would like to thank the referee, Anthony P. Marston, for a critical reading of our manuscript and suggestions that improved our model and the presentation of the results. The authors are grateful for financial support provided by Dirección General de Asuntos del Personal Académico, Universidad Nacional Autónoma de México, through grants Programa de Apoyo a Proyectos de Investigación e Innovación Tecnológica IA100720 and a IN107019. PJH also thanks Consejo Nacional de Ciencias y Tecnología, México for a research studentship. This work has made extensive use of NASA's Astrophysics Data System. The authors thank Christophe Morisset for helping with the implementation of pyCloudy and a critical reading of the manuscript. This work makes use of *Herschel*, *Spitzer* and *WISE* IR observations. *Herschel* is an ESA space observatory with science instruments provided by European-led Principal Investigator consortia and with important participation from NASA. The *Spitzer* Space Telescope was operated by the Jet Propulsion Laboratory, California Institute of Technology under a contract with NASA. Support for this work was provided by NASA through an award issued by JPL/Caltech. *WISE* is a joint project of the University of California (Los Angeles, USA) and the JPL/Caltech, funded by NASA.

DATA AVAILABILITY

The data underlying this article will be shared on reasonable request to the corresponding author.

REFERENCES

- Bailer-Jones C. A. L., Rybizki J., Fouesneau M., Mantelet G., Andrae R., 2018, *AJ*, **156**, 58
- Bianchi S., et al., 2019, *A&A*, **631**, A102
- Cherchneff I., 2013, in Kervella P., Le Bertre T., Perrin G., eds, EAS Publications Series Vol. 60, EAS Publications Series. pp 175–184 ([arXiv:1303.2805](#)), doi:10.1051/eas/1360020
- Chiavassa A., Haubois X., Young J. S., Plez B., Josselin E., Perrin G., Freytag B., 2010, *A&A*, **515**, A12
- Chu Y. H., 1981, *ApJ*, **249**, 195
- Chu Y. H., Treffers R. R., 1981, *ApJ*, **249**, 586
- Cohen M., Barlow M. J., 1975, *Astrophys. Lett.*, **16**, 165
- De Donder E., Vanbeveren D., van Bever J., 1997, *A&A*, **318**, 812
- Draine B. T., 2003, *ARA&A*, **41**, 241
- Ekström S., et al., 2012, *A&A*, **537**, A146
- Esteban C., Vilchez J. M., Smith L. J., Manchado A., 1991, *A&A*, **244**, 205
- Esteban C., Vilchez J. M., Smith L. J., Clegg R. E. S., 1992, *A&A*, **259**, 629
- Esteban C., Mesa-Delgado A., Morisset C., García-Rojas J., 2016, *MNRAS*, **460**, 4038
- Ferland G. J., et al., 2017, *Rev. Mex. Astron. Astrofis.*, **53**, 385
- Fernández-Martín A., Vilchez J. M., Pérez-Montero E., Candian A., Sánchez S. F., Martín-Gordón D., Riera A., 2013, *A&A*, **554**, A104
- Gail H.-P., Duschl W. J., Ferrarotti A. S., Weis K., 2005, **332**, 323
- Georgy C., Ekström S., Meynet G., Massey P., Levesque E. M., Hirschi R., Eggenberger P., Maeder A., 2012, *A&A*, **542**, A29
- Gómez-Llanos V., Morisset C., Szczerba R., García-Hernández D. A., García-Lario P., 2018, *A&A*, **617**, A85
- Gräfener G., Koesterke L., Hamann W.-R., 2002, *A&A*, **387**, 244
- Greenberg J. M., Li A., 1996, *A&A*, **309**, 258
- Groenewegen M. A. T., et al., 2011, *A&A*, **526**, A162
- Grosdidier Y., Moffat A. F. J., Acker A., 1998, *Ap&SS*, **260**, 181
- Gvaramadze V. V., Kniazev A. Y., Fabrika S., 2010, *MNRAS*, **405**, 1047
- Hamann W.-R., Gräfener G., Liermann A., 2006, *A&A*, **457**, 1015
- Hamann W.-R., et al., 2019, *arXiv e-prints*,
- Henning T., 2010, *ARA&A*, **48**, 21
- Iaconi R., Maeda K., De Marco O., Nozawa T., Reichardt T., 2019, *MNRAS*, **489**, 3334
- Ivanova N., et al., 2013, *A&ARv*, **21**, 59
- Kashi A., Soker N., 2010, *arXiv e-prints*, [p. arXiv:1011.1222](#)
- Kervella P., Perrin G., Chiavassa A., Ridgway S. T., Cami J., Haubois X., Verhoelst T., 2011, *A&A*, **531**, A117
- Kochanek C. S., 2011, *ApJ*, **743**, 73
- Langer N., 1995, in van der Hucht K. A., Williams P. M., eds, IAU Symposium Vol. 163, Wolf-Rayet Stars: Binaries; Colliding Winds; Evolution. p. 15
- Lü G., Zhu C., Podsiadlowski P., 2013, *ApJ*, **768**, 193
- Luri X., et al., 2018, *A&A*, **616**, A9
- Marchenko S. V., Moffat A. F. J., Crowther P. A., 2010, *ApJ*, **724**, L90
- Marston A. P., 1991, *ApJ*, **366**, 181
- Mason B. D., Hartkopf W. I., Gies D. R., Henry T. J., Helsel J. W., 2009, *AJ*, **137**, 3358
- Mathis J. S., Rimpl W., Nordsieck K. H., 1977, *ApJ*, **217**, 425
- Mathis J. S., Cassinelli J. P., van der Hucht K. A., Prusti T., Wesselius P. R., Williams P. M., 1992, *ApJ*, **384**, 197
- Merrill P. W., 1938, *PASP*, **50**, 350
- Minkowski R., 1946, *PASP*, **58**, 305
- Morisset C., 2006, in Barlow M. J., Méndez R. H., eds, IAU Symposium Vol. 234, Planetary Nebulae in our Galaxy and Beyond. pp 467–468 ([arXiv:astro-ph/0605400](#)), doi:10.1017/S1743921306003772
- Morisset C., 2014, in Asymmetrical Planetary Nebulae VI Conference. p. 62
- Morris P. W., Gull T. R., Hillier D. J., Barlow M. J., Royer P., Nielsen K., Black J., Swinyard B., 2017, *ApJ*, **842**, 79
- Nota A., 1999, Anisotropic Outflows from LBVs and Ofpe/WN9 Stars. p. 62, doi:10.1007/BFb0106356
- Nota A., Clampin M., Sirianni M., Greenfield P., Golimowski D. A., 1995, in van der Hucht K. A., Williams P. M., eds, IAU Symposium Vol. 163, Wolf-Rayet Stars: Binaries; Colliding Winds; Evolution. p. 78
- Perek L., Kohoutek L., 1967, *Bulletin of the Astronomical Institutes of Czechoslovakia*, **18**, 252
- Podsiadlowski P., Joss P. C., Hsu J. J. L., 1992, *ApJ*, **391**, 246
- Podsiadlowski P., Ivanova N., Justham S., Rappaport S., 2010, *MNRAS*, **406**, 840
- Rate G., Crowther P. A., 2020, *MNRAS*, **493**, 1512
- Reyes-Pérez J., Morisset C., Peña M., Mesa-Delgado A., 2015, *MNRAS*, **452**, 1764
- Sana H., et al., 2012, *Science*, **337**, 444
- Scicluna P., Siebenmorgen R., Wesson R., Blommaert J. A. D. L., Kasper M., Voshchinnikov N. V., Wolf S., 2015, *A&A*, **584**, L10
- Siebenmorgen R., Voshchinnikov N. V., Bagnulo S., 2014, *A&A*, **561**, A82
- Sirianni M., Nota A., Pasquali A., Clampin M., 1998, *A&A*, **335**, 1029
- Smith L. F., Aller L. H., 1969, *ApJ*, **157**, 1245
- Smith J. D. T., et al., 2007, *PASP*, **119**, 1133
- Solf J., Carsenty U., 1982, *A&A*, **116**, 54
- St-Louis N., Sévigny M., Drissen L., Martin T., 2017, in Eldridge J. J., Bray J. C., McClelland L. A. S., Xiao L., eds, IAU Symposium Vol. 329, The Lives and Death-Throes of Massive Stars. pp 446–446, doi:10.1017/S1743921317003155
- Stock D. J., Barlow M. J., 2010, *MNRAS*, **409**, 1429
- Toalá J. A., Arthur S. J., 2011, *ApJ*, **737**, 100
- Toalá J. A., Guerrero M. A., Ramos-Larios G., Guzmán V., 2015, *A&A*, **578**, A66
- Toalá J. A., et al., 2018, *ApJ*, **869**, L11
- Ueta T., Meixner M., 2003, *ApJ*, **586**, 1338
- Vamvatira-Nakou C., Hutsemékers D., Royer P., Waelkens C., Groenewegen M. A. T., Barlow M. J., 2016, *app*, **588**, A92
- Verhoelst T., van der Zypen N., Hony S., Decin L., Cami J., Eriksson K., 2009, *A&A*, **498**, 127
- Weingartner J. C., Draine B. T., 2001, *ApJ*, **548**, 296
- Weis K., 2001, *Reviews in Modern Astronomy*, **14**, 261
- Wellstein S., Langer N., Braun H., 2001, *A&A*, **369**, 939

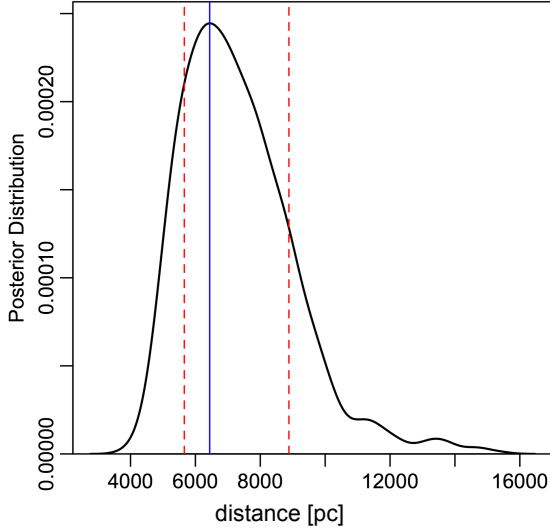


Figure A1. Posterior distribution for WR 124. The peak of the curve (blue vertical line) corresponds to the most likely distance to the star, $6.4^{+2.45}_{-0.80}$ kpc, and the red dashed lines denote the one-sigma errors.

de Mink S. E., Sana H., Langer N., Izzard R. G., Schneider F. R. N., 2014, *ApJ*, 782, 7
 van Buren D., McCray R., 1988, *ApJ*, 329, L93
 van den Heuvel E. P. J., Heise J., 1972, *Nature Physical Science*, 239, 67

APPENDIX A: DISTANCE TO WR 124

Recently, [Rate & Crowther \(2020\)](#) used *Gaia* Data Release 2 (DR2) parallaxes and Bayesian methods to obtain distance estimates to 383 Galactic Wolf-Rayet stars. Their Bayesian prior relates these massive stars to the Galactic distribution of H II regions and also takes into account extinction using a Galactic dust model. *G*-band photometry is used to correct potential underestimates of the parallax uncertainty. For WR 124 the uncorrected parallax uncertainty is $\sigma_\omega = 0.036$ mas, while the uncertainty taking into account the *G*-band magnitude is not very different, $\sigma_\omega = 0.045$. Using this method, [Rate & Crowther \(2020\)](#) obtained a distance $5.9^{+1.48}_{-1.08}$ kpc to WR 124.

For the runaway Wolf-Rayet star WR 124, which is not associated with any H II region and is far from the Galactic plane ($b > 3^\circ$), choosing a prior that is based on the Galactic distribution of H II regions does not obviously have any advantages compared to the purely geometric model of [Bailer-Jones et al. \(2018\)](#), where the prior varies smoothly as a function of Galactic longitude and latitude according to a model for the distribution of stars in the Galaxy.

In this paper, we estimate the distance to WR 124 using the *Gaia* DR2 parallaxes and also the proper motions, and employ Bayesian methods that take into account the correlations between the parallax, proper motions and their uncertainties ([Luri et al. 2018](#)). We correct for the parallax zero point using the measured QSO global zero point value of -0.029 mas ([Luri et al. 2018](#)). We use the Python and R-code routines from the tutorial⁸ described in Section 5.4 of [Luri et al. \(2018\)](#), and include the prior over distance

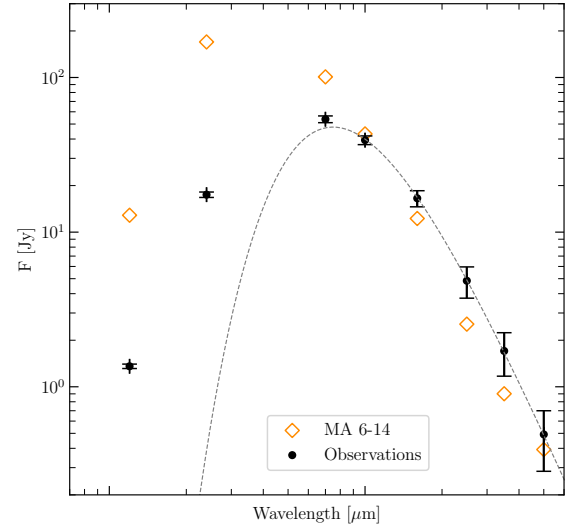


Figure B1. SED obtained from the IR observations of M 1-67 (black) dots (see Table 2). The error bars take into account uncertainties associated with the instrument calibration and the background subtraction process. The synthetic SED obtained from our model MA 06-14, is also shown with empty green diamonds (see Section 4.2 for details).

$P(r)$ given by the geometric model of [Bailer-Jones et al. \(2018\)](#) mentioned above. The posterior distribution is sampled numerically using an MCMC algorithm and the results are shown in Figure A1.

The most likely distance to WR 124 corresponds to the peak of the posterior distribution, $d = 6.4^{+2.45}_{-0.80}$ kpc, and the one-sigma errors (indicated by the red dashed lines in Fig. A1) give the credible interval of distance values. Our estimated distance is consistent, within the one-sigma error range, with the [Rate & Crowther \(2020\)](#) value.

APPENDIX B: EMISSION FROM ISM SIZE DISTRIBUTION OF SILICATE GRAINS

Model MA 6-14 (see § 4.2), which has a standard ISM distribution of silicate grains, results in the SED shown in Figure B1. There is an excess of IR emission at short wavelengths, which is due to hot small dust grains.

⁸ <https://github.com/agabrown/astrometry-inference-tutorials/tree/master/3d-distance>